

Tailoring the Edge Structure of Molybdenum Disulfide toward Electrocatalytic Reduction of Carbon Dioxide

Pedram Abbasi,[†] Mohammad Asadi,[†] Cong Liu,[‡] Soroosh Sharifi-Asl,[†] Baharak Sayahpour,[†] Amirhossein Behranginia,[†] Peter Zapol,[‡] Reza Shahbazian-Yassar,[†] Larry A. Curtiss,[‡] and Amin Salehi-Khojin^{*,†}

[†]Department of Mechanical and Industrial Engineering, University of Illinois at Chicago, Chicago, Illinois 60607, United States

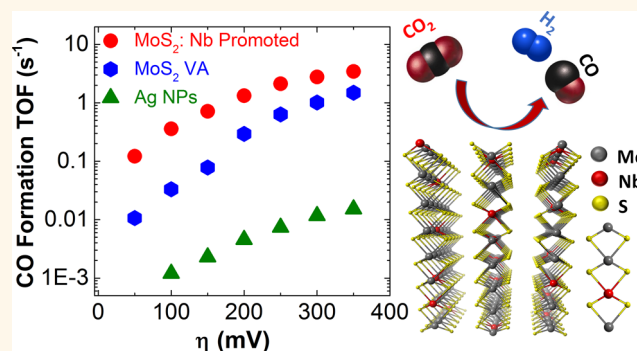
[‡]Materials Science Division, Argonne National Laboratory, Argonne, Illinois 60439, United States

S Supporting Information

ABSTRACT: Electrocatalytic conversion of carbon dioxide (CO₂) into energy-rich fuels is considered to be the most efficient approach to achieve a carbon neutral cycle. Transition-metal dichalcogenides (TMDCs) have recently shown a very promising catalytic performance for CO₂ reduction reaction in an ionic liquid electrolyte. Here, we report that the catalytic performance of molybdenum disulfide (MoS₂), a member of TMDCs, can be significantly improved by using an appropriate dopant. Our electrochemical results indicate that 5% niobium (Nb)-doped vertically aligned MoS₂ in ionic liquid exhibits 1 order of magnitude higher CO formation turnover frequency (TOF) than pristine MoS₂ at an overpotential range of 50–150 mV.

The TOF of this catalyst is also 2 orders of magnitude higher than that of Ag nanoparticles over the entire range of studied overpotentials (100–650 mV). Moreover, the *in situ* differential electrochemical mass spectrometry experiment shows the onset overpotential of 31 mV for this catalyst, which is the lowest onset potential for CO₂ reduction reaction reported so far. Our density functional theory calculations reveal that low concentrations of Nb near the Mo edge atoms can enhance the TOF of CO formation by modifying the binding energies of intermediates to MoS₂ edge atoms.

KEYWORDS: electrocatalysis, CO₂ reduction reaction, transition-metal dichalcogenides, atomic doping, ionic liquid



The advancement in the electrocatalysis science could provide an efficient way to convert carbon dioxide (CO₂) into hydrocarbon fuels that is known as the most promising approach to reach to the carbon neutral cycle.^{1–3} Recently, the potential for transition-metal dichalcogenides (TMDCs) to serve as highly efficient catalysts for electrocatalytic reduction of CO₂ has been demonstrated by our group.^{4,5} The edge states of TMDCs in contact with ionic liquid (IL) electrolytes offer a paradigm for CO₂ reduction, which takes advantage of materials with low work function, significant overlap of the d-band partial density of states with the Fermi energy, and an electrolyte “solvent” that carries CO₂ to active site efficiently.⁵ This unique combination of TMDCs and IL demonstrates remarkable catalytic activity for CO₂ reduction reaction, far exceeding the performance of state-of-the-art metal catalysts.

Unlike noble metals the rate-determining step of CO₂ reduction reaction for TMDCs/IL catalytic system is CO* desorption rather than COOH* formation⁵ that hinders the

CO formation turnover frequency (TOF). In this study, we investigate whether modifying the electronic structure of active edge atoms within an IL environment could tailor the binding strength and desorption rate of key intermediates during the CO₂ reduction reaction. An optimal condition can potentially lead to a Sabatier effect resulting in an increased TOF.^{6–8}

One promising approach to tune the electronic properties of edge atoms is to use proper dopants near the edge structures. Our previous studies showed that the Mo edge states are mainly responsible for the high catalytic performance of bulk MoS₂ in the IL electrolyte. Thus, increasing the number of these active sites could lead to an enhanced activity of the catalyst, meanwhile allowing to precisely study the effect of doping on the edge structure rather than basal plane of MoS₂.^{4,5}

Received: September 21, 2016

Accepted: December 7, 2016

Published: December 7, 2016

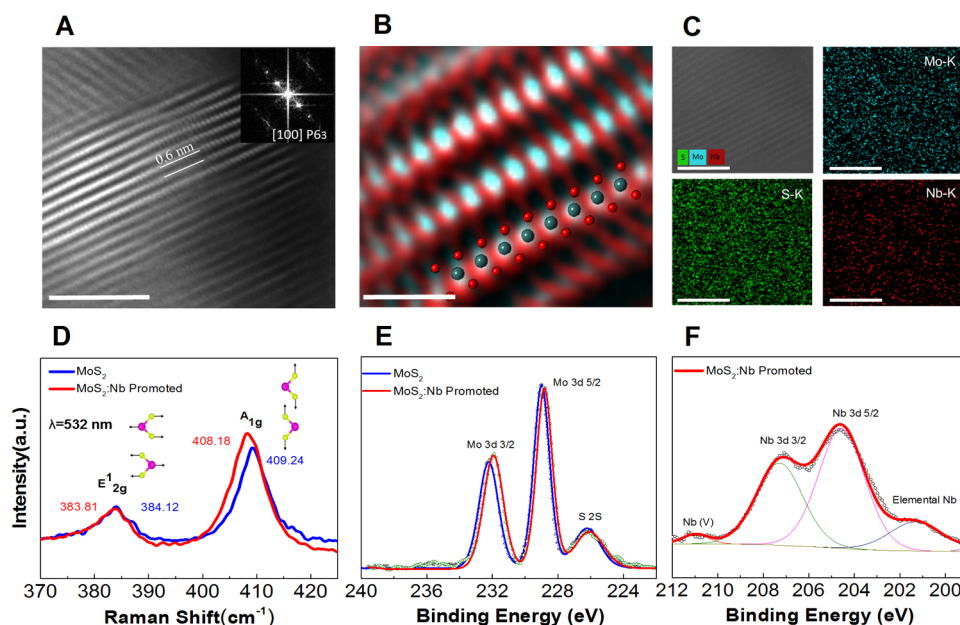


Figure 1. Structural and chemical analyses of VA-Mo_{0.95}Nb_{0.05}S₂ (MoS₂:Nb). (A) Filtered HRTEM image of the MoS₂:Nb with the corresponding FFT in the inset. Scale bar is 5 nm. (B) RGB added image constructed from (green + blue) HAADF and (red) inverted ABF image. Scale bar is 1 nm. (C) EDS maps Mo–K series, Nb–K series, and S–K series measured from the same region of the MoS₂:Nb sample. Scale bars are 5 nm. (D) Raman spectra of MoS₂:Nb and pristine MoS₂. (E) XPS scan of the Mo 3d and S 2s core-levels measured from the MoS₂:Nb and pristine MoS₂. (F) XPS scan of the Nb 3d core-level measured from the MoS₂:Nb and pristine MoS₂.

In this study, we selected vertically aligned MoS₂ (VA-MoS₂) as a model structure with nanometer level thickness (~20 nm) and surface area mainly covered by Mo terminated edge atoms.^{9–11} Niobium (Nb) and Tantalum (Ta) were selected as dopants since they can form NbS₂ (TaS₂) covalent bonds within the MoS₂ lattice in the presence of sulfur atoms without altering its lattice parameters.¹² Substitutional doping is also feasible in this structure since the Mo, Nb, and Ta oxidation states in the corresponding sulfate structures are identical.¹³ NbS₂ and TaS₂ have lattice parameters that are quite similar to MoS₂. For instance, the in-plane lattice constants of NbS₂ and TaS₂ sheets are only 0.15 Å longer than those of the MoS₂.^{13,14} However, their electronic properties are relatively different from those of MoS₂ due to the different number of valence electrons for the Mo and Nb (Ta) atoms. Nb and Ta possess one valence electron fewer compared to Mo, which makes the valence band of NbS₂ and TaS₂ half filled.^{12,14} Hence, they exhibit a metallic behavior, as opposed to the semiconducting behavior of MoS₂. It is hypothesized that this metallic behavior will enable NbS₂ and TaS₂ doping to enhance the Mo active edge atoms for CO₂ reduction.

RESULTS AND DISCUSSION

Synthesis and Characterization Methods. To test this hypothesis, VA-MoS₂ and Ta and Nb-doped MoS₂ catalysts (Mo_{1-x}M_xS₂, M = Nb and Ta) with different doping levels were synthesized using chemical vapor deposition (CVD) method.^{15–17} In brief, a thin layer of molybdenum (2.5 nm) was deposited on the glassy carbon substrates by electron beam evaporation using metal targets. Different thicknesses of Nb and Ta dopant metals (ranging from 0.5 to 5 nm) were also deposited on the top of the first layer of Mo, followed by another 2.5 nm of Mo on the top of the film in order to achieve a sandwich-like film. The thickness of the samples was confirmed by atomic force microscopy (AFM) after each

deposition. Next, the metal film substrates were sulfurized in 850 °C for 15 min in 5 mTorr by CVD method. Finally, the growth chamber was cooled down to ambient temperature under the protection of Ar gas flow, and samples were taken out for further experiments (SI, Section S1). Characterization results presented in Figure 1 are for the VA-Mo_{0.95}Nb_{0.05}S₂ structure that exhibits the best CO₂ electrochemical performance. Characterization results for other synthesized samples are presented in (SI, Sections S2–S5).

Figure 1A shows the filtered Cs corrected (spherical aberration corrected) high-angle annular dark-field (HAADF) image, resolving atomic structure of a VA-MoS₂ nanosheet with a hexagonal structure (P63/mmc) in [100] zone axis. CVD grown VA-MoS₂ structures are single crystalline nanosheets (~20 nm in diameter), aligned perpendicularly with respect to the substrate. The RGB image (Figure 1B), which is constructed from HAADF and annular bright-field (ABF) images, demonstrates the grown structure's atomic arrangement with heavy (Nb/Mo) and light (S) elements. This result is in complete agreement with the atomic model of hexagonal MoS₂ extracted from Crystal Maker software.^{4,18} In the RGB image, the signal from heavy elements (Nb/Mo) is stronger compared to S element. One should note that atomic resolution HAADF images cannot differentiate Nb and Mo due to their close atomic number of 41 and 42, respectively. Therefore, to analyze the distribution of the element Nb in the VA-Mo_{0.95}Nb_{0.05}S₂ structure, energy dispersive spectroscopy (EDS) mapping was performed on the same area to verify the homogeneous distribution of Nb in the sample (Figure 1C). Based on atomic resolution observations and EDS elemental mapping results, CVD grown nanosheets of VA-Mo_{0.95}Nb_{0.05}S₂ are highly crystalline and preserve the original hexagonal structure of MoS₂ with 0.6 nm interlayer distance. As such, Nb dopants are successfully inserted into the MoS₂ crystalline structure without

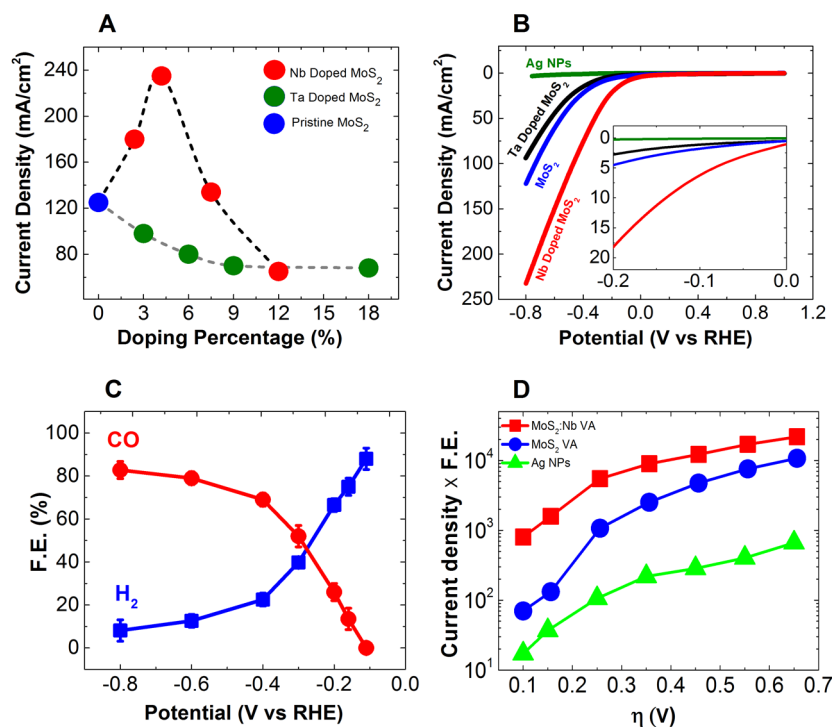


Figure 2. CO₂ reduction performance of pristine and doped MoS₂ samples. (A) Current density as a function of dopant percentage for Nb-doped and Ta-doped MoS₂ samples. (B) CV curves for Ag NPs, VA-MoS₂, VA-Mo_{0.97}Ta_{0.03}S₂, and VA-Mo_{0.95}Nb_{0.05}S₂ in CO₂ environment. (C) CO and H₂ Faradaic efficiency (FE%) at different applied potentials for VA-Mo_{0.95}Nb_{0.05}S₂. (D) CO formation partial current density for Ag nanoparticles, VA-MoS₂, and VA-Mo_{0.95}Nb_{0.05}S₂.

introducing structural modification and/or defect formation in the structure.

Raman spectroscopy was also employed to compare the structural properties of the pristine VA-MoS₂ and VA-Mo_{0.95}Nb_{0.05}S₂ samples (Figure 1D). The Raman spectrum of Mo_{0.95}Nb_{0.05}S₂ does not exhibit any major differences from that of the pristine VA-MoS₂. Two identical peaks at 384 and 409 cm⁻¹ confirm that the VA-MoS₂ structure is not considerably affected by dopants.^{19,20} However, a closer look reveals small differences between the pristine and doped structure. A shift in the characteristic A_{1g} band by ~1 cm⁻¹ from the VA-MoS₂ (409 cm⁻¹) reveals a slight effect of doping on the *c*-axis vibration mode.²¹

X-ray photoelectron spectroscopy (XPS) has been carried out to provide an exact stoichiometric ratio and binding energy shift of doped elements in all of the synthesized samples. Figure 1E shows the results of Mo 3d and S 2s core levels of VA-Mo_{0.95}Nb_{0.05}S₂ and pristine VA-MoS₂. Binding energies (BEs) of all peaks were calibrated on the C–C bond of C 1s at 284.8 eV. In the case of Mo_{0.95}Nb_{0.05}S₂ structure, we observed a distinguishable shift toward lower binding energies only in Mo 3d spectra, but not in C 1s or O 1s spectra. This shift is a strong evidence of the substitutional doping of Nb atoms into the MoS₂ structure as a result of p-type doping. Figure 1F also shows the Nb 3d core levels of Mo_{0.95}Nb_{0.05}S₂. The peaks on 204.5 and 207.2 eV in Nb 3d spectra are attributed to the reduced Nb atoms in the MoS₂ structure, and two other peaks on the binding energies of 201.2 and 210.7 eV correspond to elemental Nb and Nb₂O₅ on the surface that are in agreement with previous reports on fullerene-like (IF) Nb_xMo_{1-x}S₂ nanoparticles.^{21,22}

Electrochemical Experiments. The CO₂ reduction performance of the synthesized catalysts was studied by

different electrochemical experiments. Cyclic voltammetry (CV) experiments were performed inside a two-compartment three-electrode electrochemical cell at the potential range of +1.0 to -0.8 V vs reversible hydrogen electrode (RHE, all potentials in this study reported based on RHE) with 20 mV/s scan rate. Previously, we uncovered that MoS₂/IL catalytic system is a proton limited system due to the high density of d electrons on Mo edge atoms.^{4,23} Thus, all experiments were performed using CO₂ saturated electrolyte composed of 50 vol % 1-ethyl-3-methylimidazolium tetrafluoroborate (EMIM-BF₄) and 50 vol % of deionized water that exhibits the lowest pH (3.2) among different concentrations of water/IL.^{4,24} This composition of the electrolyte provides the highest concentration of protons in the system resulting in the maximum CO₂ reduction rate. Figure 2A shows the CO₂ reduction current density as a function of different Nb and Ta dopant concentrations at the potential of -0.8 V. The current densities are normalized according to the geometrical surface area.^{4,20,25} Results show a volcano effect in the catalytic activity of VA-Mo_{1-x}Nb_xS₂. In particular, the current density increases from 121 mA/cm² for pristine VA-MoS₂ to 180 mA/cm² for VA-Mo_{0.97}Nb_{0.03}S₂ and then reaches its highest value at 237 mA/cm² for VA-Mo_{0.95}Nb_{0.05}S₂. After this doping level, increasing the dopant concentration resulted in reduced activity in which current densities of 137 and 72 mA/cm² were obtained for VA-Mo_{0.92}Nb_{0.08}S₂ and VA-Mo_{0.88}Nb_{0.12}S₂, respectively.

Ta-doped MoS₂ catalysts were also studied as another candidate to promote the catalytic performance of MoS₂. However, at all doping levels, the catalytic performance of VA-Mo_{1-x}Ta_xS₂ was lower than that for pristine VA-MoS₂. In particular, current densities of 98, 82, 71, and 68 mA/cm² were obtained for doped samples of VA-Mo_{0.97}Ta_{0.03}S₂, VA-Mo_{0.94}Ta_{0.06}S₂, VA-Mo_{0.91}Ta_{0.09}S₂, and VA-Mo_{0.82}Ta_{0.18}S₂, re-

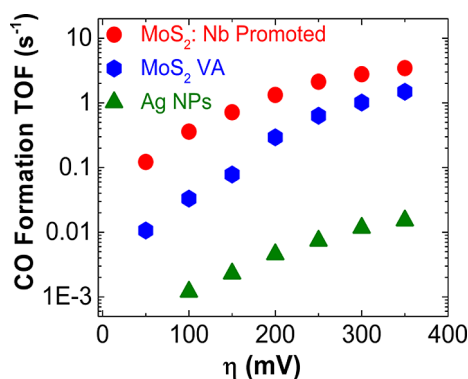


Figure 3. Calculated CO formation TOF at different applied overpotentials for VA-Mo_{0.95}Nb_{0.05}S₂, pristine VA-MoS₂, and Ag nanoparticles.

spectively. Our XPS results (SI, Section S3) indicate a doublet of Ta on 25.78 and 24.50 eV which exhibits a relative shift on 4f 7/2 oxidation state from its distinguishable TaS₂ (IV) reference peak at 23.60 eV by ~ 0.9 eV.²⁶ We speculate that this change in the binding energy of Ta atoms with the host structure could result in a deviation from the optimal electronic properties of doped structure that may underperform the electrocatalytic activity for CO₂ reduction reaction.

Based on the CV results (Figure 2A), the rest of this study is mainly focused on the Mo_{0.95}Nb_{0.05}S₂ catalyst which exhibits the best electrocatalytic performance for CO₂ reduction among all studied catalysts. In Figure 2B, the activity of Mo_{0.95}Nb_{0.05}S₂ catalyst was compared with pristine VA-MoS₂, VA-Mo_{0.97}Ta_{0.03}S₂, and Ag nanoparticles (Ag NPs) in the 50 vol % EMIM-BF₄ IL. The CV results indicate that at the potential of -0.8 V, the current density of Mo_{0.95}Nb_{0.05}S₂ (237 mA/cm²) is approximately 2 and 50 times higher than that of VA-MoS₂ and Ag NPs, respectively. The inset of Figure 2B also shows the current density of the studied catalysts at lower potentials (0 to -0.2 V vs RHE). At -0.2 V, the current density of Mo_{0.95}Nb_{0.05}S₂ is 19 mA/cm², which is more than 4 and 70 times higher than that of VA-MoS₂ (4.5 mA/cm²) and Ag NPs (0.26 mA/cm²), respectively. Detail of CV experiments are presented in (SI, Section S6).

The selectivity of Mo_{0.95}Nb_{0.05}S₂ was also studied using gas chromatograph (GC) equipped with a thermal conductivity detector (SI, Section S7). The overall Faradaic efficiency (FE) measurements indicate that this catalyst produces a tunable

mixture of CO and H₂ ranging from 12% to 82% of CO formation at the range of studied potentials -0.16 to -0.8 V. Figure 2D shows the CO formation partial current density of the catalysts which is defined as CO formation FE% multiplied by the CO₂ reduction current density. As seen from Figure 2D, the CO formation current density of Mo_{0.95}Nb_{0.05}S₂ has been improved by an order of magnitude at the low overpotentials of 0–150 mV. VA-Mo_{0.95}Nb_{0.05}S₂ catalyst also exhibits approximately 2 orders of magnitude higher catalytic activity over Ag NPs at the all range of overpotentials.²⁴ Our measurements at the potential of -0.8 V indicate the formation rate of 2.23×10^{-8} and 1.98×10^{-9} (molmin⁻¹ cm⁻²) for CO and H₂, respectively.

Next, the CO formation TOF of the catalysts was calculated from the capacitive method²⁷ in which the activity of the catalysts is normalized based on the number of active sites. We measured the double-layer capacitance (C_{dl}) and calculated the roughness factor (RF) to obtain the number of active sites for each catalyst (SI, Section S8).²⁸ Our measurements show a C_{dl} of 4.18, 2.74, and 3.71 mF/cm² for VA-Mo_{0.95}Nb_{0.05}S₂, VA-MoS₂, and Ag NPs resulting in 8.06×10^{16} , 5.28×10^{16} , and 4.44×10^{17} number of active sites, respectively. The results indicate a 1.5-fold increase of the number of active sites in the surface morphology of the pristine MoS₂ catalyst as a result of Nb doping. This is consistent with AFM results in which ~ 2 times more roughness (RMS) was observed for VA-Mo_{0.95}Nb_{0.05}S₂ compared with VA-MoS₂ (SI, Section S5). Figure 3 shows the calculated CO formation TOF of these catalysts as well as Ag NPs. Results indicate that MoS₂ exhibits approximately 1 and 2 orders of magnitude higher CO formation TOF at low overpotentials (100–300 mV) than pristine VA-MoS₂ and Ag NPs, respectively. For instance, at the overpotential of 100 mV, TOF values of 0.36, 0.033, and 0.0012 S¹⁻ have been calculated for VA-Mo_{0.95}Nb_{0.05}S₂, VA-MoS₂, and Ag NPs, respectively.

We also studied the CO formation onset potential to obtain a better perspective on catalytic performance of VA-Mo_{0.95}Nb_{0.05}S₂ and a criteria to compare this catalytic system with state of the art catalysts for CO₂ reduction reaction (CO₂ RR). In this context, *in situ* differential electrochemical mass spectrometry (DEMS) was used to measure the onset potential of CO₂ reduction reaction. To increase the accuracy of the measurement, the experiments were performed in a pure IL EMIM-BF₄ to eliminate possible effects of hydrogen evolution reaction. The potential was swept between $+0.6$ and -0.8 V vs

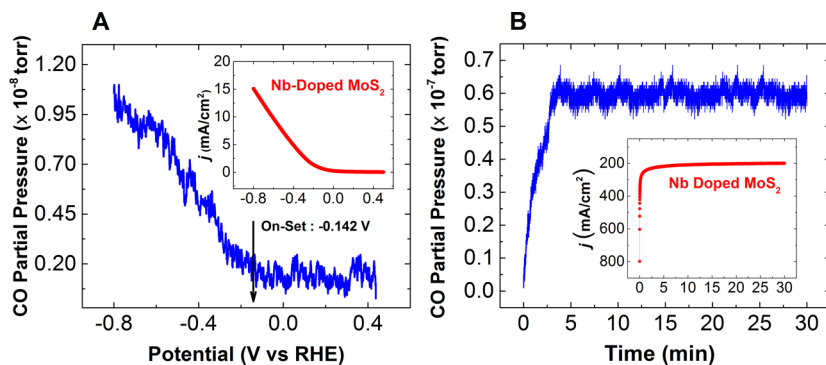


Figure 4. Differential electrochemical mass spectrometry results. CO partial pressure vs applied potential for VA-Mo_{0.95}Nb_{0.05}S₂ during (A) the CV inside pure IL (EMIM-BF₄) and (B) CA experiment at the potential of -0.8 V vs RHE inside 50 vol % EMIM-BF₄ and 50 vol % water. Insets shows the corresponding CV and CA results.

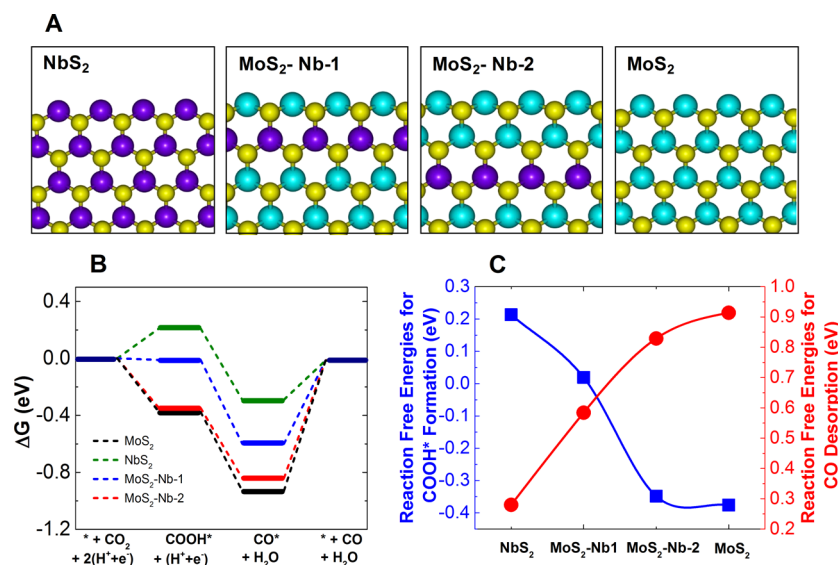


Figure 5. DFT results. (A) Schematic of Nb-doped MoS₂ structures with different position of dopant. (B) Reaction pathways of CO₂ → CO on MoS₂, NbS₂, and Nb-doped MoS₂ edges. Nb-doped MoS₂ was constructed by replacing the second row of Mo atoms (MoS₂-Nb-1) and the third row of Mo atoms (MoS₂-Nb-2) from the edge with Nb atoms. The catalytic reaction pathways were calculated on the metal edge of each material, with the adsorbate coverage of 1 ML. (C) Trends of COOH* formation energies and CO desorption energies on the bare metal edge of different systems.

RHE with a low scan rate of 1 mV/s to make it possible to measure pressure fluctuations in the chamber as a function of applied potential. In particular, the variation of CO partial pressure was monitored to detect any product formation during the applied potential. As shown in Figure 4A, the partial pressure variation of CO increases with the applied potential following the CV plot trend. The recorded onset potential of -0.142 V for VA-Mo_{0.95}Nb_{0.05}S₂ catalyst is only 31 mV higher than the thermodynamic value of CO₂ reduction reaction onset potential (-0.11 V *vs* RHE), which is two times smaller than pristine MoS₂ catalyst (61 mV). This clearly indicates that VA-Mo_{0.95}Nb_{0.05}S₂ is the most energy efficient system for synthesis gas production compared with other catalysts reported so far.^{4,29–32}

The partial pressure variation of CO was also monitored during chronoamperometry (CA) experiments at the potential of -0.8 V using DEMS. Figure 4B shows the corresponding DEMS results for 30 min continuous CA experiments inside 50 vol % EMIM-BF₄ and 50 vol % of deionized water, confirming the continuous and stable production rate of CO. The recorded current density for VA-Mo_{0.95}Nb_{0.05}S₂ is 202 mA/cm² at the potential of -0.8 V *vs* RHE (inset of Figure 4B), which is $\sim 14\%$ less than CV results (238 mA/cm²). The differences are attributed to the capacitive behavior in CV experiments.⁵

Computational Results. Density functional theory (DFT) calculations were carried out to investigate the effect of Nb in the Mo_{1-x}M_xS₂ structure shown in Figure 5. In particular, the electrocatalytic pathways of CO₂ reduction to CO were compared on the metallic edges of pure NbS₂ and MoS₂ as well as the Mo_{1-x}Nb_xS₂. Our calculations showed that the Nb edge of the pure NbS₂ is catalytically less favorable than the Mo edge of the pure MoS₂. NbS₂ has an endergonic step to form the first intermediate, COOH*. This would engender a higher overpotential (estimated from the reaction free energy of the rate-limiting electrochemical step) than MoS₂, in which the formations of COOH* and CO* are both exergonic. However, MoS₂ has a stronger binding with the product, CO, which

could slow down CO desorption (CO* → CO + *) and, thus, decrease the turnover. On the other hand, doping Nb atoms near the Mo edge of MoS₂ (Figure 5, Mo_{1-x}Nb_xS₂ configurations 1 and 2) would decrease the binding strength between the Mo edge and CO, while keeping the formation of COOH* and CO* exergonic. This suggests that Nb-doped MoS₂ could lead to a faster turnover for CO desorption than pure MoS₂. This result can explain the lower onset potential of CO formation in Nb-doped MoS₂ compared to the pristine structure. The trend of CO binding strengths can be attributed to differences in the electronic structures of the systems. The evidence for this is the density of states of the d orbitals of the edge metal atoms (SI, Figure S12 and Table S4). Our calculations show that the d-band center of Nb in NbS₂ is 0.27 eV, while that of Mo in MoS₂ is -0.33 eV. Doping Nb into the near-edge of MoS₂ results in the shift of the edge Mo d-band center toward a less negative value (-0.29 eV), which leads to a weakened binding of CO. However, higher doping concentrations of Nb may also have an opposite effect on the catalytic performance due to the increased work function of Mo_{1-x}Nb_xS₂ at high Nb concentrations, which could lead to poorer electron-transfer properties for the electrochemical reduction of CO₂. These two competing effects of Nb as a dopant may account for the dependence of the experimental results on the amount of dopant, *i.e.*, improved catalytic performance of MoS₂ at low Nb doping concentrations ($< \sim 5\%$) and decreased performance at a higher Nb doping concentration ($> \sim 5\%$). The DFT results for Ta-doped MoS₂ (SI, Figure S13) suggest that the doping of Ta into the second Mo row of MoS₂ could lead to an unfavorable reaction pathway, *i.e.*, the formation of COOH* becomes endergonic. Although pure TaS₂ seems to have reasonable reaction pathways, the higher work function of this material (5.5 eV compared to 5.0 eV of MoS₂) would still be a drawback for its electron-transfer property. Thus, the DFT calculations showed that unlike Nb-doped MoS₂, Ta-doped MoS₂ is not likely to

have a good “trade-off” effect between the reaction energetics and the work function.

CONCLUSIONS

In summary, using CVD method, we synthesized VA-Mo_{1-x}M_xS₂ (M = Nb and Ta) structures and tested their electrocatalytic performance for CO₂ reduction reaction. We found a volcano-like trend for the catalytic performance of VA-Mo_{1-x}Nb_xS₂, with the highest CO₂ reduction activity for VA-Mo_{0.95}Nb_{0.05}S₂. The CO formation TOF of this structure indicated 1 order of magnitude higher overall performance compared to pristine VA-MoS₂ in the range of 50–150 mV overpotential. The CO formation TOF of this catalyst was also 2 orders of magnitude better than Ag NPs catalyst over the entire range of overpotentials (0–650 mV).²⁴ Moreover, this structure showed the lowest CO₂ reduction reaction onset overpotential (31 mV) measured by *in situ* DEMS. However, our results showed negative effect of doping on the catalytic performance of all studied Ta-doped VA-Mo_{1-x}Ta_xS₂ structures. This study indicated that the presence of proper dopants in the structure of MoS₂ can significantly improve the catalytic performance of MoS₂. The ability to embed the dopants into the atomic structure of the catalysts could open a promising route to enhance the catalytic performance of the edge atoms by modifying their electronic properties.

METHODS AND EXPERIMENTAL SECTION

Material Synthesis. Vertically aligned pristine, Ta and Nb-doped MoS₂ catalysts were synthesized using chemical vapor deposition (CVD) method. Substrates (glassy carbon) were thoroughly cleaned by rinsing in acetone, methanol, and isopropanol (IPA) solvents, sequentially followed by drying in a nitrogen flow. Electron beam evaporation (Varian Evaporation System) was used to deposit different thicknesses of metals (Mo, Nb, and Ta) on the substrates using metal targets (Purchased from Kurt J. Lesker). Metal deposited substrates were loaded in the center of a three-zone furnace (MTI Corp. model OTF-1200X) with precise thermometer and gas flow meters. The sulfur precursor (Sigma-Aldrich) was placed in the first zone of the chamber where the maximum temperature reaches to 200 °C. The center of the furnace was heated to 850 °C in 60 min and kept constant for next 15 min to activate the metal surface for sulfurization process. Argon (Ar) gas was continuously flown (200 sccm) during this growth process. Finally, growth chamber was cooled down to ambient temperature under the protection of Ar gas flow, and samples were taken out for further experiments.

The Ag NP solution was made by mixing 10 mg of silver nanopowder (>100 nm diameter, Aldrich) with 600 μL of ultrapure water, 600 μL of isopropyl alcohol, and 10 μL of 1100EW 5% Nafion solution (DuPont). The mixture was then coated on glassy carbon after 3 min of sonication.

X-ray Photoelectron Spectroscopy (XPS). XPS experiments were carried out using a Thermo Scientific ESCALAB 250Xi instrument. The instrument was equipped with an electron flood and scanning ion gun. All spectra were calibrated to the C 1s binding energy at 284.8 eV. To quantify the atomic concentration of each element, all data have been processed by Thermo Avantage software.

Scanning Transmission Electron Microscopy (STEM). Atomic resolution imaging and EDS analysis were performed using an aberration corrected JEOL ARM200CF equipped with a cold field emission gun and 1.2 Å spatial resolution and an Oxford X-max 100TLE windowless X-ray detector. A 22 mrad probe convergence angle was used to perform STEM. HAADF detector with 90 mrad inner-detector angle was utilized to obtain Z contrast images. Also to identify S atoms, ABF detector with 7–14 mrad collection angle was used. Sample preparation was done by transferring CVD grown doped and undoped samples into IPA solution. After sonication for 20 min,

solution was drop casted onto the lacy carbon TEM grid. Sample was lamped for another 20 min before loading to JEOL double tilt holder. Crystal Maker software was also used to generate schematic image of the crystalline structure.

Raman Characterization. The data are obtained with a HORIBA LabRAM HR Evolution confocal Raman microscope. The instrument was configured with a 532 nm laser source, 1200 g/mm grating, a Horiba Andor detector, and a 100× objective. Laser powers at the sample were between 1 and 15 mW. Acquisition time, averaging parameters, and ND filters were optimized for the best signal-to-noise ratio.

Atomic Forced Microscopy (AFM) characterization. Experiments carried out using Bruker-Nano AFM instrument. Samples were carefully washed by acetone and IPA before experiment to remove any impurity. Root mean square roughness (Rq) of the doped and undoped samples has been measured by Gwyddion software.

Electrochemical Methods. All electrochemical experiments were performed by a two-compartment three-electrode electrochemical cell to perform CO₂ reduction reaction. Platinum (Pt) gauze 52 mesh (Alfa Aesar) and Ag/AgCl (BASi) were used as counter and reference electrodes, respectively. The cathode and anode part of the cell were separated through ion exchange membrane to eliminate the effect of product oxidation at the anode surface. A pure CO₂ gas (99.99%, Praxair) was bubbled into the 50 vol % IL solution (EMIM-BF₄ and water) for 30 min prior to each experiment. The cell was connected to the potentiostat (CH Instruments) for electrolysis characterization. Product characterization was carried out using an SRI 8610C GC system equipped with 72 × 18 in. S.S. molecular sieve-packed column and a thermal conductivity detector. Ultrahigh-purity helium and nitrogen gases (purchased from Praxair) were used as the carrier gas for CO and H₂ detection, respectively. For product characterization, chronoamperometry measurements have been performed for a desired duration of time (~15 min), and 1 mL samples were taken out from the dead volume of the cell using a lock-in syringe (Hamilton) and injected into the gas chromatography system under identical conditions. Faradaic efficiency measurements were calculated based on the mole fractions of injected samples corresponding to calibration curves and applied potential (details of faradic efficiency measurements are presented in SI, Section S7).

Differential Electrochemical Mass Spectrometry (DEMS) Measurements. The DEMS experiment was performed with a quadrupole detector purchased from (Hiden Analytical Inc.). A two-compartment three-electrode cell was designed with the total volume of 20 cc for a better detection of evolved products. The cell was carefully sealed with rubber septa and sealant before each experiment. The pure CO₂ (99.99%) was continuously bubbled into the IL electrolyte. A magnet bar has been used to stir the electrolyte to avoid the effect of mass transfer. The head space volume was about 8 mL during the experiment. The cell was under ultrahigh-vacuum pressure (1 × 10⁻⁸ Torr) during the mass spectroscopy analysis. The product stream was injected from head space of the cell to the DEMS using quartz coated very low flow capillary line. The potential was swept between +0.6 to -0.8 V vs RHE with the scan rate of 1 mV/s to provide enough time for measuring pressure fluctuations in the chamber. The variation of CO partial pressure was then monitored to detect any product formation during the applied potential.

Density Functional Theory (DFT) Details. Periodic DFT calculations were performed using the PBE functional with plane wave basis sets in VASP package.^{33,34} Single-layer nanoribbons of the TMDCs with zigzag edges were constructed to mimic the nanostructures for the reaction free energies calculations. For the nanoribbons, each unit cell includes 8 × 1 atoms and 16 S atoms, containing both the metal and the S edges. A 15 Å vacuum space is set both on top of the metal edge and between two nanoribbon periodic images. A kinetic energy cutoff of 400 eV was used for all the calculations, and K-points grids of 3 × 1 × 1 were used for the energy calculations of the nanoribbons. Γ-point was used for gas-phase molecules. All the calculations involving the nanoribbons are spin-polarized calculations.

ASSOCIATED CONTENT

Supporting Information

The Supporting Information is available free of charge on the ACS Publications website at DOI: 10.1021/acsnano.6b06392.

Additional experimental details and data (PDF)

AUTHOR INFORMATION

Corresponding Author

*E-mail: salehikh@uic.edu.

ORCID

Pedram Abbasi: 0000-0001-6835-3062

Soroosh Sharifi-Asl: 0000-0003-0441-9231

Baharak Sayahpour: 0000-0003-0200-6636

Peter Zapol: 0000-0003-0570-9169

Author Contributions

A.S.K., P.A., and M.A. conceived the idea. P.A. and M.A. performed the electrochemical experiments. P.A. and A.B. grew and synthesized the experimental samples. P.A. and B.S. did the characterizations. S.S. and R.S. carried out STEM and EELS. A.S.K. supervised P.A., M.A., and B.S., and A.B. L.C., C.L., and P.Z. carried out DFT calculations.

Notes

The authors declare no competing financial interest.

ACKNOWLEDGMENTS

A.S.K. work was supported by National Science Foundation (grant no. NSF-CBET-1512647). The authors acknowledge the MRSEC Materials Preparation and Measurement Laboratory shared user facility at the University of Chicago (grant no. NSF-DMR-1420709). The authors also acknowledge the EPIC facility (NUANCE Center, Northwestern University), which has received support from the MRSEC program (NSF DMR-1121262) at the Materials Research Center; the Nanoscale Science and Engineering Center (NSF EEC-0647560) at the International Institute for Nanotechnology; and the State of Illinois, through the International Institute for Nanotechnology. The work at Argonne National Laboratory was supported by the U.S. Department of Energy under contract DE-AC0206CH11357 from the Division of Materials Science and Engineering, Basic Energy Science (P. Z., C.L., and L.A.C.). R.S.Y and S.S.A. acknowledge the financial support from NSF DMR-1620901.

REFERENCES

- (1) Davis, S. J.; Caldeira, K.; Matthews, H. D. Future CO₂ Emissions and Climate Change from Existing Energy Infrastructure. *Science* **2010**, *329*, 1330–1333.
- (2) Haszeldine, R. S. Carbon Capture and Storage: How Green Can Black Be? *Science (Washington, DC, U. S.)* **2009**, *325*, 1647–1652.
- (3) Lastoskie, C. Caging Carbon Dioxide. *Science* **2010**, *330*, 595–596.
- (4) Asadi, M.; Kumar, B.; Behranginia, A.; Rosen, B. a.; Baskin, A.; Repnin, N.; Pisasale, D.; Phillips, P.; Zhu, W.; Haasch, R.; Klie, R. F.; Král, P.; Abiade, J.; Salehi-Khojin, A. Robust Carbon Dioxide Reduction on Molybdenum Disulfide Edges. *Nat. Commun.* **2014**, *5*, 4470.
- (5) Asadi, M.; Kim, K.; Liu, C.; Addepalli, A. V.; Abbasi, P.; Yasaei, P.; Phillips, P.; Behranginia, A.; Cerrato, J. M.; Haasch, R.; Zapol, P.; Kumar, B.; Klie, R. F.; Abiade, J.; Curtiss, L. A.; Salehi-Khojin, A. Nanostructured Transition Metal Dichalcogenide Electrocatalysts for CO₂ Reduction in Ionic Liquid. *Science* **2016**, *353*, 467–470.
- (6) Cheng, J.; Hu, P. Utilization of the Three-Dimensional Volcano Surface to Understand the Chemistry of Multiphase Systems in Heterogeneous Catalysis. *J. Am. Chem. Soc.* **2008**, *130*, 10868–10869.
- (7) Nørskov, J. K.; Bligaard, T.; Hvolbaek, B.; Abild-Pedersen, F.; Chorkendorff, I.; Christensen, C. H. The Nature of the Active Site in Heterogeneous Metal Catalysis. *Chem. Soc. Rev.* **2008**, *37*, 2163–2171.
- (8) Rosen, B. a.; Salehi-Khojin, a.; Thorson, M. R.; Zhu, W.; Whipple, D. T.; Kenis, P. J. a.; Masel, R. I. Ionic Liquid-Mediated Selective Conversion of CO₂ to CO at Low Overpotentials. *Science* **2011**, *334*, 643–644.
- (9) Wang, H.; Tsai, C.; Kong, D.; Chan, K.; Abild-pedersen, F.; Nørskov, J. K.; Cui, Y. Transition-Metal Doped Edge Sites in Vertically Aligned MoS₂ Catalysts for Enhanced Hydrogen Evolution. *Nano Res.* **2015**, *8*, 566–575.
- (10) Kong, D.; Wang, H.; Cha, J. J.; Pasta, M.; Koski, K. J.; Yao, J.; Cui, Y. Synthesis of MoS₂ and MoSe₂ Films with Vertically Aligned Layers. *Nano Lett.* **2013**, *13*, 1341–1347.
- (11) Yu, Y.; Huang, S.-Y.; Li, Y.; Steinmann, S. N.; Yang, W.; Cao, L. Layer-Dependent Electrocatalysis of MoS₂ for Hydrogen Evolution. *Nano Lett.* **2014**, *14*, 553–558.
- (12) Tedstone, A. A.; Lewis, D. J.; O'Brien, P. Synthesis, Properties, and Applications of Transition Metal-Doped Layered Transition Metal Dichalcogenides. *Chem. Mater.* **2016**, *28*, 1965–1974.
- (13) Ding, Y.; Wang, Y.; Ni, J.; Shi, L.; Shi, S.; Tang, W. First Principles Study of Structural, Vibrational and Electronic Properties of Graphene-like MX₂ (M = Mo, Nb, W, Ta; X = S, Se, Te) Monolayers. *Phys. B* **2011**, *406*, 2254–2260.
- (14) Ivanovskaya, V. V.; Zobelli, A.; Gloter, A.; Brun, N.; Serin, V.; Colliex, C. Ab Initio Study of Bilateral Doping within the MoS₂-NbS₂ System. *Phys. Rev. B: Condens. Matter Mater. Phys.* **2008**, *78*, 134104.
- (15) Laskar, M. R.; Ma, L.; Kannappan, S.; Sung Park, P.; Krishnamoorthy, S.; Nath, D. N.; Lu, W.; Wu, Y.; Rajan, S. Large Area Single Crystal (0001) Oriented MoS₂. *Appl. Phys. Lett.* **2013**, *102*, 252108.
- (16) Wang, H.; Kong, D.; Johanes, P.; Cha, J. J.; Zheng, G.; Yan, K.; Liu, N. MoSe₂ and WSe₂ Nano Flms with Vertically Aligned Molecular Layers on Curved and Rough Surfaces. *Nano Lett.* **2013**, *13*, 3426–3433.
- (17) Ma, L. Corrigendum: Zaozao Qui. *ChemPlusChem* **2014**, *79*, n/a.
- (18) Zhou, W.; Zou, X.; Najmaei, S.; Liu, Z.; Shi, Y.; Kong, J.; Lou, J.; Ajayan, P. M.; Yakobson, B. I.; Idrubo, J. C. Intrinsic Structural Defects in Monolayer Molybdenum Disulfide. *Nano Lett.* **2013**, *13*, 2615–2622.
- (19) Lee, C.; Yan, H.; Brus, L. E.; Heinz, T. F.; Hone, J.; Ryu, S. Anomalous Lattice Vibrations of Single- and Few-Layer MoS₂. *ACS Nano* **2010**, *4*, 2695–2700.
- (20) Kibsgaard, J.; Chen, Z.; Reinecke, B. N.; Jaramillo, T. F. Engineering the Surface Structure of MoS₂ to Preferentially Expose Active Edge Sites for Electrocatalysis. *Nat. Mater.* **2012**, *11*, 963–969.
- (21) Suh, J.; Park, T. E.; Lin, D. Y.; Fu, D.; Park, J.; Jung, H. J.; Chen, Y.; Ko, C.; Jang, C.; Sun, Y.; Sinclair, R.; Chang, J.; Tongay, S.; Wu, J. Doping against the Native Propensity of MoS₂: Degenerate Hole Doping by Cation Substitution. *Nano Lett.* **2014**, *14*, 6976–6982.
- (22) Deepak, F. L.; Cohen, H.; Cohen, S.; Feldman, Y.; Popovitz-Biro, R.; Azulay, D.; Millo, O.; Tenne, R. Fullerene-like (IF) Nb_xMO_{1-x}S₂ Nanoparticles. *J. Am. Chem. Soc.* **2007**, *129*, 12549–12562.
- (23) Rosen, B. a.; Zhu, W.; Kaul, G.; Salehi-Khojin, A.; Masel, R. I. SI-Water Enhancement of CO₂ Conversion on Silver in 1-Ethyl-3-Methylimidazolium Tetrafluoroborate. *J. Electrochem. Soc.* **2013**, *160*, H138–H141.
- (24) Salehi-Khojin, A.; Jhong, H. R. M.; Rosen, B. A.; Zhu, W.; Ma, S.; Kenis, P. J. A.; Masel, R. I. Nanoparticle Silver Catalysts That Show Enhanced Activity for Carbon Dioxide Electrolysis. *J. Phys. Chem. C* **2013**, *117*, 1627–1632.
- (25) Jaramillo, T. F.; Jørgensen, K. P.; Bonde, J.; Nielsen, J. H.; Horch, S.; Chorkendorff, I. Identification of Active Edge Sites for

Electrochemical H₂ Evolution from MoS₂ Nanocatalysts. *Science* **2007**, *317*, 100–102.

(26) Ettema, A. R. H. F.; Haas, C. An X-Ray Photoemission Spectroscopy Study of Interlayer Charge Transfer in Some Misfit Layer Compounds. *J. Phys.: Condens. Matter* **1993**, *5*, 3817–3826.

(27) Benck, J. D.; Chen, Z.; Kuritzky, L. Y.; Forman, A. J.; Jaramillo, T. F. Amorphous Molybdenum Sulfide Catalysts for Electrochemical Hydrogen Production: Insights into the Origin of Their Catalytic Activity. *ACS Catal.* **2012**, *2*, 1916–1923.

(28) Li, D. J.; Maiti, U. N.; Lim, J.; Choi, D. S.; Lee, W. J.; Oh, Y.; Lee, G. Y.; Kim, S. O. Molybdenum sulfide/N-Doped CNT Forest Hybrid Catalysts for High-Performance Hydrogen Evolution Reaction. *Nano Lett.* **2014**, *14*, 1228–1233.

(29) Kumar, B.; Asadi, M.; Pisasale, D.; Sinha-Ray, S.; Rosen, B. a; Haasch, R.; Abiade, J.; Yarin, A. L.; Salehi-Khojin, A. Renewable and Metal-Free Carbon Nanofibre Catalysts for Carbon Dioxide Reduction. *Nat. Commun.* **2013**, *4*, 2819.

(30) Lu, Q.; Rosen, J.; Zhou, Y.; Hutchings, G. S.; Kimmel, Y. C.; Chen, J. G.; Jiao, F. A Selective and Efficient Electrocatalyst for Carbon Dioxide Reduction. *Nat. Commun.* **2014**, *5*, 3242.

(31) Chen, Y.; Li, C. W.; Kanan, M. W. Aqueous CO₂ Reduction at Very Low Overpotential on Oxide-Derived Au Nanoparticles. *J. Am. Chem. Soc.* **2012**, *134*, 19969–19972.

(32) Li, C. W.; Kanan, M. W. CO₂ Reduction at Low Overpotential on Cu Electrodes Resulting from the Reduction of Thick Cu₂O Films. *J. Am. Chem. Soc.* **2012**, *134*, 7231–7234.

(33) Kresse, G.; Furthmüller, J. Efficient Iterative Schemes for Ab Initio Total-Energy Calculations Using a Plane-Wave Basis Set. *Phys. Rev. B: Condens. Matter Mater. Phys.* **1996**, *54*, 11169–11186.

(34) Kresse, G.; Furthmüller, J. Efficiency of Ab-Initio Total Energy Calculations for Metals and Semiconductors Using a Plane-Wave Basis Set. *Comput. Mater. Sci.* **1996**, *6*, 15–50.